Probing the depth of Jupiter's Great Red Spot with the Juno gravity experiment

M. Parisi [a,*], E. Galanti [a], S. Finocchiaro [b], L. Iess [b], Y. Kaspi [a]

[a] Department of Earth and Planetary Sciences, Weizmann Institute of Science, 234 Herzl st., 76100 Rehovot, Israel
[b] Dipartimento di Ingegneria Meccanica e Aerospaziale, Sapienza Università di Roma, via Eudossiana 18, 00184 Rome, Italy

ABSTRACT

Jupiter's Great Red Spot (GRS) is the most dominant and long-lived feature in Jupiter's atmosphere. However, whether this is a shallow atmospheric feature or a deeply rooted vortex has remained an open question. In this study, we assess the possibility of inferring the depth of the GRS by the upcoming *Juno* gravity experiment. This is achieved by an exploration of the possible gravitational signature of the vortex by systematically extending the surface winds into the interior and analyzing the resulting gravity signal. The gravity anomaly is then compared to the expected accuracy in the retrieval of the surface gravity at the GRS location obtained with numerical simulations of the Doppler data inversion based on the expected trajectory of the spacecraft. Starting from observations of the atmospheric velocity at the cloud level, we project the wind using a decay scale height along coaxial cylinders parallel to the spin axis and explore a wide range of decay scale heights in the radial direction. Assuming the large scale vortex dynamics are geostrophic, and therefore thermal wind balance holds, the density anomaly distribution due to Jupiter's winds can be derived from the velocity maps. The novelty of this approach is in the integration of thermal wind relations over a three-dimensional grid, and in the inclusion of the observed meridional velocity as measured during the Cassini flyby of Jupiter. The perturbations in the mean zonal flow give rise to non zero tesseral spherical harmonics in Jupiter's gravitational potential. We provide an estimate of this asymmetric gravity coefficients for different values of the wind decay scale height. We conclude that the mass anomaly associated with the GRS is detectable by the *Juno* gravity experiment if the vortex is deep, characterized by a vertical height larger than 2,000 km below the cloud level of Jupiter, and that the large mass involved with deep winds does not render much the ability to measure the feature.

© 2015 Elsevier Inc. All rights reserved.

1. Introduction

The Great Red Spot is a perpetual anticyclone that has become an icon of Jupiter's atmosphere ever since it was first observed in 1665 by Gian Domenico Cassini. For this reason, the study of this perpetual vortex remains a crucial driver and scientific objective for future space missions to the giant planet. In this regard, *Juno* has the earliest possibility of observing the spot and answering some fundamental questions about its interior structure. Telescopic and spacecraft observations in the last decades not only suggest that the anticyclone evolution moves towards a more circular shape, but also show that it is shrinking. Asay-Davis et al. (2009) show that, between 1996 and 2006, the surface extension of the vortex has diminished by 15%, while its peak velocity remained constant. More recently, analysis of 2014 Hubble spectral imaging data has highlighted that the GRS size has reached its historical minimum (Simon et al., 2014). It is not known whether this condition is due to the damping of the vortex intensity or to periodic oscillations. In any case, the fortunate timing underlines the necessity for the *Juno* mission to collect as much data as possible.

Choi et al. (2007) have measured the surface velocity vectors of the GRS using an automated cloud tracking algorithm applied to *Galileo* images. They report measurements of the high velocity collar of the vortex, with peak velocities of 170 ms^{-1}. Although observations of Jupiter's winds at the cloud-level are largely available, the penetration of the flow motion at depth, including the GRS, is unknown and object of a long-lasting controversy. The argument, extensively reviewed by Vasavada and Showman (2005), can be summarized as whether the jets are shallow and therefore involve only the upper layers of the atmosphere, or extend deeply into Jupiter's interior, organizing in differentially rotating coaxial deep-rotating cylinders (Busse, 1976; Ingersoll

* Corresponding author.

and Pollard, 1982). The only existent *in situ* measurements of the deep wind dynamics come from the *Galileo Entry Probe* which penetrated the jovian atmosphere at 6.5°N latitude (Young, 1998). The probe reached pressure levels down to 22 bar, detecting strong eastward zonal winds characterized by velocities of up to 160 ms^{-1}. Yet, these data only reach down to about 0.2% of Jupiter's mean radius, excluding information about the underlying layers. Furthermore, the vertical structure of the vortex might be decoupled from that of the jets, reaching deeper or shallower layers of Jupiter's atmosphere than the surroundings.

Using *Voyager* imaging observations, Dowling and Ingersoll (1988) calculate the absolute vertical vorticity on Jupiter's GRS by looking at the horizontal velocity field. Using conservation of shallow-layer potential vorticity, they conclude that, since the ratio of relative vorticity to local thickness must be conserved, there must be deeper circulation beneath the GRS, although still constrained to very surficial layers. In the same study, the authors argue for the shallow vertical extension of the vortex by pointing out that in the proximity of the GRS, the absolute vorticity, and thus the thickness density, varies by a factor of two along closed streamlines. Dowling and Ingersoll (1989) use a two-layer model in which a deeper, zonally symmetric steady atmosphere is overlaid by a thin weather-layer, and show that it is possible to produce long-lasting vortices, such as the GRS. Morales-Juberias and Dowling (2013) show that coherent stable GRS-like features, with an appearance very similar to the observed GRS, appear in a 3D atmospheric general circulation model (GCM), which extends only down to 10 bars. These models all assume that instabilities generating vortices are confined to the upper layers of the gaseous planet. However, as shallow geostrophic turbulence is characterized by an inverse cascade to large-scale coherent structures (Rhines, 1979), the existence of such vortices in these models does not rule out the possibility that in reality the GRS is deeply rooted.

It is therefore possible that the GRS extent is tied to the surrounding zonal flows which might be very deep. One argument for this is that if the GRS was indeed a shallow feature, the vortex would have a much shorter life span since it would be sheared by the strongly turbulent atmospheric flows surrounding it (like storms on Earth). Yano and Flierl (1994) show in a parameterized deep QG model that in order to remain stable over long time scales the GRS must be deep, and therefore argue for a strong coupling between the GRS and the deep convective dynamics of the interior. Liu and Schneider (2010) generate long-lived coherent vortices in an idealized shallow GCM, and suggest that the life span of a vortex increases with the radiative time scale which, in turn, increases with pressure, whence with vertical extent. Therefore a scenario in which the phenomenon is deep-rooted is also plausible. In addition, it should be noted that shallow forcing can result in deep jets and vortices (Showman et al., 2006; Lian and Showman, 2008), and similarly deep forcing can result in shallow features (Kaspi et al., 2009), so the question of what is forcing the GRS may be decoupled from whether the GRS is deep or shallow. The *Juno* gravity experiment might hold the key to learning more about the depth of the GRS.

In this study we assess the possibility of detecting the gravitational signature of Jupiter's main cyclone by exploiting very precise measurements of the planet's gravitational potential (Finocchiaro and Iess, 2010; Finocchiaro, 2013), that can be linked to the amount of mass involved in the vortex and, by extension, to its depth. Furthermore, compared to previous studies looking at the gravity signature of dynamics on Jupiter (Kaspi et al., 2010; Kaspi, 2013; Liu et al., 2013; Kong et al., 2013), here we consider full three-dimensional maps of Jupiter's wind velocity without limiting the analysis to zonally axisymmetric profiles.

In Section 2 we report on the process of building three-dimensional maps of Jupiter's winds. We start from longitudinal mosaics of the planet's velocity vector retrieved by Choi and Showman (2011) by processing *Cassini* imaging data, and proceed by propagating the surface profile in the direction parallel to Jupiter's rotation axis (Busse, 1976; Hubbard, 1999). Since this propagation depth is unknown, we introduce a free parameter which is the e-folding decay scale height of the winds *H*, which then allows to cover a wide range of cases ranging from deep barotropic winds to winds that rapidly decay with radius (Kaspi et al., 2010, 2013). We continue in Section 3 by introducing the thermal wind balance as applied for a deep atmosphere (Kaspi, 2008; Kaspi et al., 2009), considering here the balance both in the zonal and meridional directions. Starting from the fundamental equations we obtain the expression for planetary density anomalies generated by zonal and meridional wind motions, assuming that a reference hydrostatic state is known.

In Section 4 we present numerical results for the density perturbations and contributions to the gravitational potential of the planet, and analyze the effects of varying the decay scale height on the redistribution of Jupiter's mass due to fluid dynamics. In Section 5 we investigate the gravity signature for cases where the vertical scales for the vortices and the background zonal velocity field are different. In Section 6 we discuss the possibility of detecting the gravitational signature of the GRS given the capabilities of the *Juno* gravity experiment, considering a varying scale height for the wind penetration. We compare the magnitude of the anomalies generated with our model of Jupiter's atmospheric dynamics to the expected uncertainties on the retrieved surface gravity resulting from numerical simulations of the experiment (Finocchiaro and Iess, 2010; Finocchiaro, 2013).

2. Jupiter's wind velocity

Multi-spectral observations of Jupiter's atmosphere during the *Cassini* Jupiter flyby in December 2000 have provided a large amount of atmospheric data that have been analyzed by Choi and Showman (2011) in terms of cloud patterns and kinetic energy. The data set contains observation sequences acquired by the Imaging Science Subsystem (ISS). In their work, the authors provide full longitudinal maps of Jupiter's surface wind vectors by using an automated cloud feature tracker (Choi et al., 2007). The results of the cloud tracking process are shown in Fig. 1 in terms of cloud-level wind velocity. The 2D maps are generated using the CB2 filter observations, which are sensitive to pressure levels down to 1.1 bar and are referenced to Jupiter System III (Choi and Showman, 2011). The zonal (azimuthal) component of the wind velocity (Fig. 1a) shows a mostly axisymmetric structure, positive and negative values indicate eastward and westward wind, respectively. As a result the flow organizes in wide rotating bands parallel to the equatorial plane, with peaks of nearly 150 ms^{-1}. The equatorial region, comprised between 15°S and 15°N latitude, is superrotating and contributes the most to the total kinetic energy. The energetic contribution of the meridional component (Fig. 1b), is limited, except in correspondence to the main vortices and ovals, e.g., the GRS and Oval BA (28°S Lat., 82° Long.), where the meridional velocity is of order 65 and 60 ms^{-1}, respectively. Due to the low contrast and resolution at high latitudes, related to the *Cassini* flyby geometry, wind vectors poleward of 50° are either replaced by the zonally symmetric average (Fig. 1a) or omitted (Fig. 1b). Where available, maps of the wind vectors are affected by measurement noise, leading to typical uncertainties of 5 ms^{-1}, with peaks between 10 and 20 ms^{-1} (Choi and Showman, 2011). A close-up of the GRS reveals the high-speed collar of the vortex, where the magnitude of the velocity, after the removal of the zonal average, reaches values up to 95 ms^{-1} (Fig. 2), in contrast with the low-velocity inner region. The shape of the cyclone at the time of the observations is
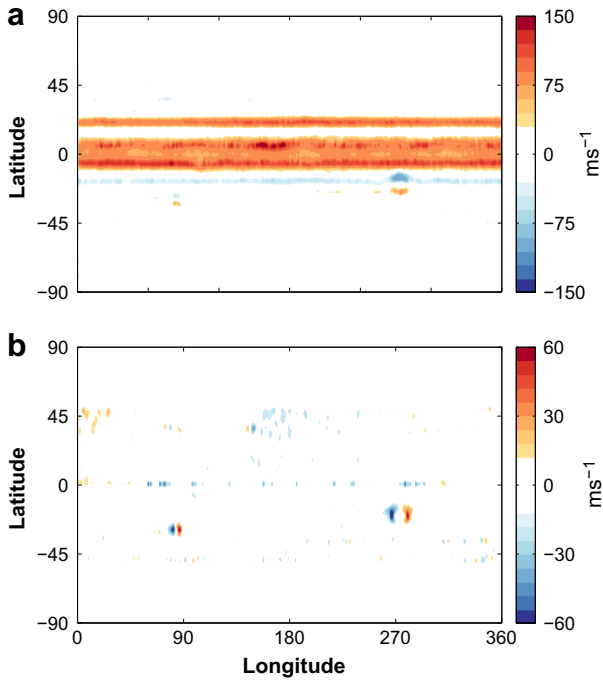
Fig. 1. Jupiter's cloud-level velocity, relative to Jupiter System III (Choi and Showman, 2011). The map of Jupiter's zonal (azimuthal) component (a) is almost axisymmetric. The meridional component (b) is, on average, an order of magnitude smaller than the zonal component. In both panels we observe large anomalies at the GRS location (22°S Lat.; 274° Long.).
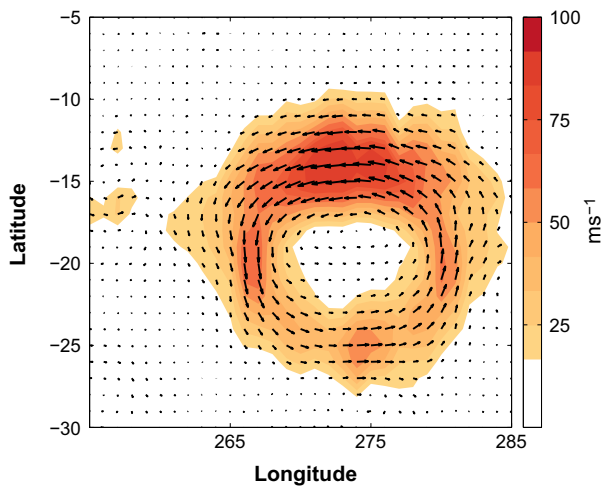
Fig. 2. Wind speed around the GRS location, after the removal of the zonal average. The wind intensity is in color, and arrows show the direction. The high-velocity collar shows peaks of 95 ms^{-1}, while the circumscribed area is characterized by very low wind speed. The vortex dimensions are about 12,000 km and 22,000 km, latitudinally and longitudinally, respectively.

elliptical, extending for about 10° latitudinally and 18° longitudinally, around Jupiter System III latitude and longitude 22°S and 274°, respectively.

In order to obtain a three-dimensional map of the wind velocity, it is necessary to make assumptions on the penetration of Jupiter's jets at depth. In particular, due to angular momentum constraints (Kaspi et al., 2009; Schneider and Liu, 2009), we assume that the surface winds are aligned with the direction parallel to the axis of rotation. In addition, we allow exponential decay of the intensity in the radial direction, so as to control the vertical penetration (Kaspi et al., 2010):

$$u(r, \theta, \phi) = u_{\text{cyl}}(r, \theta, \phi)e^{-\frac{R_J - r}{H}},$$

$$v(r, \theta, \phi) = v_{\text{cyl}}(r, \theta, \phi)e^{-\frac{R_J - r}{H}}, \tag{1}$$

where u is the zonal component of the velocity, v is the meridional component and r, θ, ϕ are the distance from the origin, latitude and longitude in Jupiter System III, respectively. The velocities $u_{\text{cyl}}, v_{\text{cyl}}$ are functions that extend the cloud level winds barotropically along the spin direction, H is the e-folding scale and R_J is Jupiter's mean radius. We also assume zero velocity in the radial direction $w(r, \theta, \phi) \equiv 0$, which is a viable assumption as long as we limit the analysis to motion that is not deep compared to the radius of the planet.[1] As the objective of this study is to estimate the gravity signal of a feature observed at the upper levels, we consider only cases where the upper level winds are extending into the interior, although a completely decoupled interior flow is also a very viable possibility (Galanti and Kaspi, 2015).

By slicing the planetary sphere along one meridian (e.g., 274° Long.), we show a latitude-depth cross-section of the wind azimuthal component (Fig. 3a–c) for various decay heights. The maps are not symmetric with respect to the equatorial plane as in Kaspi et al. (2010), instead we consider the actual latitudinal variability from pole to pole as in Kaspi (2013). The counter-rotating flows (westward and eastward) characterizing the GRS are visible around latitude 22°S. Symmetrically, we choose one latitudinal level (e.g., 22°S Lat.) and show the meridional component as a function of depth and longitude (Fig. 3d–f). Around longitude 274°, the southward and northward flows of the GRS appear. The vortex high-speed collar extends down to different depths depending on the decay scale height, for which we show three different cases, where the decay depth changes by an order of magnitude. For shallow winds (Fig. 3a and d), with a decay scale height of $H = 10^2$ km, the penetration of Jupiter's jets is very marginal, confined to less than 1% of the mean radius (note that the scale of the depth axis is logarithmic), and the portion of planetary mass involved in the wind motion is very limited. Despite the superficiality of the atmospheric dynamics, the equatorial superrotation is clearly visible in Fig. 3a and so is the other major eastward jet located at 20°N. In the intermediate depth wind case (Fig. 3b and e) with a $H = 10^3$ km, jets penetrate deeper into Jupiter's gaseous upper layers (around $0.02R_J$). To avoid discontinuities on the equatorial plane, due to the asymmetry of the wind profile with respect to the plane itself, we apply a smoothing function near the equator. The smoothing is confined to a narrow region on the equatorial plane and has no effect on the results. In the deep wind case with $H = 10^4$ km (Fig. 3c and f), the e-folding scale is about $0.15R_J$, resulting in flows involving a bigger portion of Jupiter's mass.

3. Idealized thermal wind model

Jupiter is a fast rotator and its atmospheric dynamics are characterized by very large scales. Therefore, the typical Rossby number is very small and the planet's large scale atmospheric motion, including the GRS, can be considered to be, to the leading order, in thermal wind balance (Pedlosky, 1987). For deep atmospheric flow thermal-wind balance takes the form (Kaspi et al., 2009, 2010):

$$2\Omega \cdot \nabla(\tilde{\rho}\boldsymbol{v}) = \nabla\rho' \times \boldsymbol{g}, \tag{2}$$

where Ω is the planetary rotation rate, $\boldsymbol{v}$ is the velocity vector, $\boldsymbol{g}$ is the radial gravity vector, and the density has been divided into a

---

[1] Note that if the vortex is extremely deep the flow around the vortex becomes in the radial and azimuthal direction, and therefore we set the maximum depth of the winds to be no more that the size of the width of the vortex ($O(10^4)$ km).
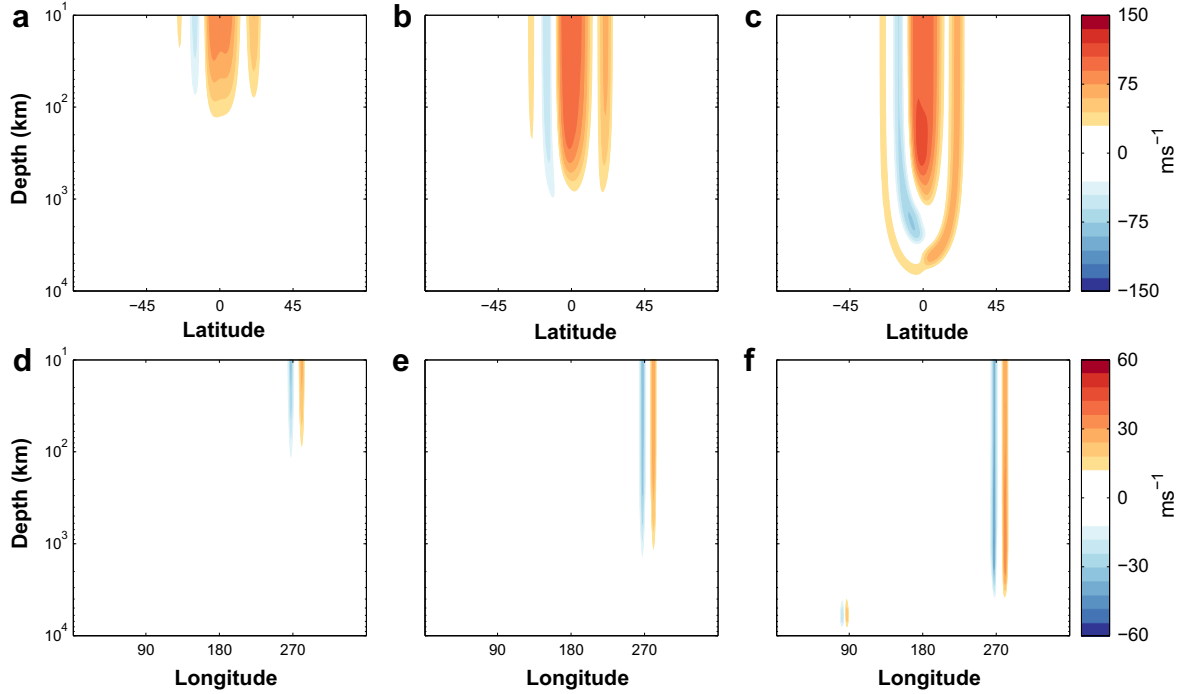
Fig. 3. Vertical sections of the zonal (top panels) and meridional (bottom panels) components of the velocity at 274° Long. and 22°S Lat., respectively, for different deacy scale heights: $H = 10^2$ km (a, d); $H = 10^3$ km (b, e); $H = 10^4$ km (c, f). The plots show the penetration at depth, defined as the distance from the cloud-level, of the GRS high-speed collar.

static component $\tilde{\rho}(r)$, and a small deviation from that, $\rho'(r, \theta, \phi)$, due to atmospheric dynamics, where r, θ and ϕ are the planetary radial direction, colatitude and longitude, respectively. We assume the effect of the planetary oblateness is small (e.g., Kong et al., 2013) for estimating the effect of the GRS dynamics on gravity, and thus perform the analysis in spherical coordinates meaning that $\tilde{\rho}$ and $\boldsymbol{g}$ are only a function of radius.[2]

The vectorial Eq. (2) can be broken into a system of scalar differential equations. The projections of the equation onto the $\hat{\phi}$ (zonal) and $\hat{\theta}$ (meridional) directions are, respectively:

$$\frac{\partial \rho'}{\partial \theta} = \frac{2\Omega r}{g}\frac{\partial \tilde{\rho} u}{\partial z},$$
$$\frac{\partial \rho'}{\partial \phi} = -\frac{2\Omega r \sin\theta}{g}\frac{\partial \tilde{\rho} v}{\partial z}, \tag{3}$$

where ρ' is the unknown variable to solve for. For convenience we denote with z the direction parallel to the spin axis, which in spherical coordinates can be further divided into derivatives in radius and colatitude (see Appendix A). Since $\boldsymbol{g}$ is parallel to $\boldsymbol{r}$, the rhs of Eq. (2) has no component in the radial direction. If we make the assumption of no flow motion in the radial direction (see Section 2) the projection of the equation on the radial direction is identically satisfied. In order to obtain an analytical expression for the density anomalies, we solve system (3) by performing two steps of integration, once over θ and once over ϕ (see Appendix A), which yields:

$$\rho'(r, \theta, \phi) = \frac{1}{2}\int\left(\frac{2\Omega}{g}r\frac{\partial \tilde{\rho} u}{\partial z}\right)d\theta$$
$$- \frac{1}{2}\int\left(\frac{2\Omega}{g}r\sin\theta\frac{\partial \tilde{\rho} v}{\partial z}\right)d\phi + \rho'_1(r, \theta) + \rho'_2(r, \phi), \tag{4}$$

[2] The gravity vector is calculated by integration of the static density $\tilde{\rho}$, and is therefore only a function of radius. Zhang et al. (2015) suggest a correction to this equation by adding a term associated with the non-radial component of the gravity vector due to dynamics. However, for the values of decay scale heights considered here such a term is small.

that can be numerically integrated, granted that the reference hydrostatic density $\tilde{\rho}(r)$ is known. In this paper we derive $\tilde{\rho}$ from 1D models by Guillot and Morel (1995). In order to calculate the constants of integration $\rho'_1(r, \theta)$ and $\rho'_2(r, \phi)$, it is necessary to impose two boundary conditions. The first that we apply is that, in case the meridional component of the velocity goes to zero ($v \to 0$), the expression for the density perturbations must converge to that of the purely zonal wind case (Kaspi et al., 2009, 2010), whence:

$$\rho'_1(r, \theta) = \frac{1}{2}\int\left(\frac{2\Omega}{g}r\frac{\partial \tilde{\rho}\bar{u}(r, \theta)}{\partial z}\right)d\theta, \tag{5}$$

where $\bar{u}(r, \theta)$ is the zonal mean velocity (see Appendix A for the full derivation).

We impose a second boundary condition to show that the second constant of integration can only be a function of the distance from the center of the planet. As the meridional component of the velocity v is close to zero at the poles (as shown by *Cassini* observations, see Fig. 1), the second equation in (3), implies that at the poles, the derivative of the density anomaly with respect to the longitude must be zero as well

$$\left(\frac{\partial \rho'}{\partial \phi}\right)_{\theta = 0, \pi} = 0. \tag{6}$$

If we look at Eq. (4), we find that for $\theta = 0, \pi$: the first term on the rhs cannot be a function of longitude because, for the mass continuity equation, if $v = 0$ then $\partial u/\partial \phi = 0$; the second term disappears because $v = 0$; the third term is only a function of r and θ; thus the only possible variations in longitude are given by ρ'_2. Nevertheless, this term cannot assume different values for different longitudes at the poles, thus in the two singular points the integration function (ρ_2) is only a function of r:

$$\left(\frac{\partial \rho'_2}{\partial \phi}\right)_{\theta = 0, \pi} = 0. \tag{7}$$

However, since ρ'_2 cannot vary with latitude, it must be independent of ϕ also distant from the poles, and:

$$\rho'_2(r,\theta) = \rho'_2(r). \tag{8}$$

The final form of the density perturbations is:

$$\rho'(r,\theta,\phi) = \frac{1}{2}\int\left(\frac{2\Omega}{g}r\frac{\partial\tilde{\rho}u}{\partial z}\right)d\theta - \frac{1}{2}\int\left(\frac{2\Omega}{g}r\sin\theta\frac{\partial\tilde{\rho}v}{\partial z}\right)d\phi$$
$$+ \frac{1}{2}\int\left(\frac{2\Omega}{g}r\frac{\partial\tilde{\rho}\bar{u}}{\partial z}\right)d\theta + \rho'_2(r). \tag{9}$$

Alternatively, one can integrate the first equation in (3) with respect to θ and end up with a constant of integration which is a function of r and ϕ, as in Kaspi et al. (2010):

$$\rho'(r,\theta,\phi) = \int\left(\frac{2\Omega}{g}r\frac{\partial\tilde{\rho}u}{\partial z}\right)d\theta + \rho'_1(r,\phi). \tag{10}$$

In Appendix A we show how, if $v \to 0$, the two solutions (9) and (10), coincide. Furthermore, by comparing the equations, it is clear that the second term on the rhs of (9) accounts for the longitudinal variations that lack in the third term, in order to balance the first term. The two approaches are equivalent and lead to the same results, since the two components of the horizontal velocity are bound by continuity, and each one carries information about the other due to the continuity of the flow.

Support for the flow being geostrophic (even locally) in the regions of the GRS, comes from integrating the observed winds (Choi and Showman, 2011) to calculate the geopotential height anomaly near the GRS given by:

$$\eta(\phi,\theta) = \frac{f}{g}\Psi(\phi,\theta), \tag{11}$$

where Ψ is the geostrophic streamfunction, f is the Coriolis parameter and g is the gravitational acceleration at the surface (Pedlosky, 1987). The results give surface elevations whose trend, in the proximity of the GRS location, is very similar to the velocity vector distribution in Fig. 3, with peaks of about 1 km above the reference pressure level of 1 bar. The result is consistent with observations of the feature in the methane filter. West and Tomasko (1980) observed the GRS to be up to $30 \pm 1\%$ brighter than the adjacent zone when using a 8900-Å filter. This observational datum suggests that the cloud top of the GRS is elevated above the surrounding to pressure levels between 0.29 and 0.87 bar.

4. Results with a uniform scale height

Our purpose is to produce a three-dimensional map of Jupiter's wind-induced density anomalies, and its surface gravity signature. To this end, given the wind profiles from Section 2, we use Eq. (9) to calculate these perturbations from the background hydrostatic density. The integrations are done with a resolution of $0.5°$, in the longitudinal and latitudinal directions, and 10 vertical levels per scale height, resulting in a denser grid towards the upper layers of the atmosphere. The starting point and the direction of the integration step do not influence the results.

The density fluctuations due to Jupiter's atmospheric dynamics affect the gravity field of the planet in different degrees and orders of the gravitational harmonics, depending on their vertical penetration. The variations in the real and imaginary components of the unnormalized spherical harmonic coefficients of Jupiter's gravitational potential are:

$$\Delta C_{lm} = \frac{1}{MR_J^l}\int_0^{R_J}r^{2+l}dr\int_0^{2\pi}\int_{-1}^1 P_l(\mu)\cos(m\phi)\rho'd\mu d\phi,$$
$$\Delta S_{lm} = \frac{1}{MR_J^l}\int_0^{R_J}r^{2+l}dr\int_0^{2\pi}\int_{-1}^1 P_l(\mu)\sin(m\phi)\rho'd\mu d\phi, \tag{12}$$

where l and m are the degree and order of the expansion, respectively, M is the mass of Jupiter, $\mu = \cos\theta$ and P_l is the Legendre Polynomial of degree l.

The density perturbations used in (12) are defined up to an arbitrary function of r (Eq. (9)). However, fortunately, this does not limit our ability to calculate accurately ΔC_{lm} and ΔS_{lm}, since it is multiplied by the Legendre polynomials $P_l(\mu)$ that are only a function of latitude with a zero mean, and therefore any part of ρ' that is independent of latitude vanishes in the integration. Thus the choice of $\rho'_2(r)$ does not affect the integration in (12), and the equations can be numerically integrated to produce the contributions of the winds to the gravity of Jupiter, being independent of this integration function.

Since $d\mu = -\sin\theta d\theta$, the contributions of the density anomalies to the overall gravity, depend on the product $\rho'\sin\theta$. In Fig. 4 we show the horizontal profile of this effective density anomaly, obtained by selecting a vertical level located 5 km below the cloud level, and a specific decay scale height ($H = 10^3$ km). The map reflects the trend of the wind velocity: the horizontal structure of the zonal jets is predominant, with the equatorial band between $15°$S and $15°$N responsible for most of the density fluctuations (with peaks of about 0.03 kg m^{-3}). However, small-scale longitudinal features such as the GRS ($274°$ Long.) and the Oval BA ($85°$ Long.) are clearly visible and identified by denser circular spots. Although the gravity calculation is invariant with respect to the choice of $\rho'_2(r)$, for the purpose of plotting $\rho'(\theta,\phi)$ in Fig. 4 we define $\rho'_2(r)$ so there are zero-mean anomalies along the latitudinal and longitudinal direction:

$$\int_\theta\int_\phi\rho'(r,\theta,\phi)d\theta d\phi = 0. \tag{13}$$

Next, we generate realizations of full 30×30 expansions using different scale heights, in terms of ΔC_{lm} (Fig. 5) and ΔS_{lm}, which both decrease with l^{-2}. The deviations of the potential from that of a rotating solid body are larger the deeper the wind penetration, because of the increasing amount of planetary mass involved in atmospheric dynamics. As a result, as the scale height increases, the ΔC_{lm} coefficients increase in absolute value. The first column of the triangle matrices (Fig. 5) represents the axisymmetric deformations of the planet due to the winds (ΔJ_n). Among them, the main contribution to the planetary gravitational potential comes from ΔJ_2, although still much smaller than the solid body contribution to the oblateness (Hubbard, 2013). The degree-2 zonal harmonic increases with H and is positive for any value of the scale height, as we expect in the presence of strong zonal winds in the equatorial region that tend to augment the oblateness of the planet (Hubbard, 1999; Kaspi et al., 2010). The presence of longitudinal variations in the wind velocity, including the vortices, produces non-zero tesseral harmonics, the non-axisymmetric part of the gravity field of Jupiter. The effect of Jupiter's atmospheric dynamics on the zonal gravity field of giant planets has been previously discussed by Kaspi et al. (2010) and Kaspi (2013). However this paper gives the first estimate of the magnitude of the fluctuations in the tesseral ($l \neq m$) gravity spectrum. The GRS, even though, by definition, a small-scale perturbation, influences the spectrum of the spherical harmonic coefficients at every degree and order.

The gravity signal coming from the winds can be quantified by considering the resulting surface gravity Δg, defined as the gravitational acceleration on a reference sphere and related to the spherical harmonic coefficients by:

$$\Delta g = -\nabla(\Delta\Phi(R_J,\theta,\phi)), \tag{14}$$

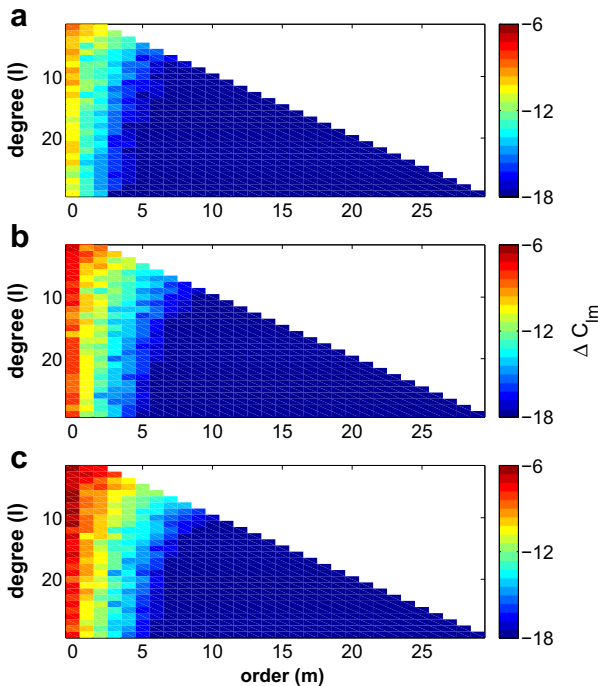where $\Delta\Phi$ is the contribution to the gravitational potential of Jupiter due to atmospheric dynamics:
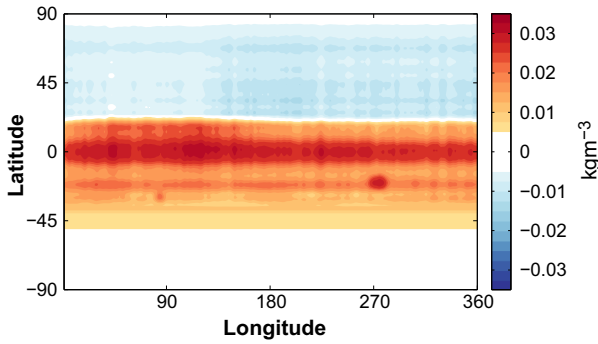
Fig. 4. A horizontal map of the density anomalies multiplied by $\sin\theta$, located 5 km below the cloud-level winds using $H = 10^3$ km. The zonal winds generate the biggest contributions to the density fluctuation. Nevertheless, the GRS anomaly (274° Long.) is visible as a localized feature characterized by denser fluid.

$$\Delta\Phi(r) = -\frac{GM_w}{r}\sum_{l>1}\left(\frac{R}{r}\right)^l\sum_{m=0}^{l}[\Delta C_{lm}Y_{lm}^C(\theta,\phi) + \Delta S_{lm}Y_{lm}^S(\theta,\phi)]. \qquad (15)$$

At the GRS location (22°S Lat., 274° Long.), we calculate the peak value of the gravity anomaly Δg generated by the GRS, as a function of the decay scale height H (Fig. 6). In order to decouple the contributions due to the zonal jets and the small-scale longitudinal features, such as the GRS, we remove the longitudinal mean of the surface gravity. The magnitude of the gravity anomaly associated with the vortex is zero if $H = 0$, then it rapidly increases with the scale height. We show results for a continuous range of decay scale heights between 10^2 km and 10^4 km.

5. Different scale heights for vortices and zonal-mean wind

In the previous sections we have applied a uniform e-folding scale in the radial direction to all velocity vectors at the

Fig. 5. The absolute value (in log scale) of the real components of Jupiter's gravitational potential expansion in spherical harmonics (ΔC_{lm}). The greatest contribution to the gravity spectrum, the ΔJ_2, is of order 10^{-8}, 10^{-6} and 5×10^{-6} for $H = 10^2$ km (panel a), $H = 10^3$ km (panel b) and $H = 10^4$ km (panel c), respectively. The coefficients become larger and the contributions from the low-degree harmonics, especially the zonals, become more predominant for larger H.
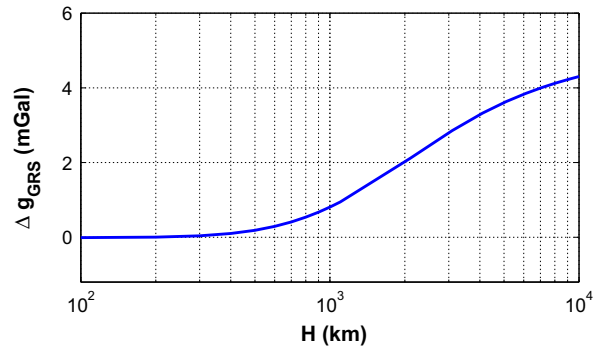
Fig. 6. Gravity anomaly generated by the GRS as a function of H, in km. The mean zonal surface gravity is removed in order to isolate the signature of the vortex. The plot is semi-logarithmic on the x-axis. The contribution of the GRS to the overall surface gravity grows very steeply with the decay scale height.

cloud-level from Choi and Showman (2011). However, the deep vertical structure of the GRS might differ from that of the background velocity field in which it is embedded. Therefore, in this section we consider different decay scale heights for Jupiter's zonally mean wind (H_1) and the deviations from these (i.e., vortices, H_2), respectively. In this scenario the GRS can extend down to different pressure levels than that of the low-latitude jets, and vice versa. This condition affects the expected gravity signal coming from the winds and introduces the possibility of assessing the likelihood for the GRS gravitational signature to be detected even in the case of shallow zonal winds. Consistently, we must also take into account cases where the jets are very deep but the vortex is confined to a thin layer of Jupiter's atmosphere.

We generate maps of the surface gravity acceleration using Eq. (14) for every combination of $H_1, H_2 = [10^2, 10^3, 10^4]$ km (Fig. 7). If the GRS and the background velocity field are both characterized by the same scale height (Fig. 7a, e, and i) the induced map of the gravity anomalies reflects the wind surface structure (compare to Figs. 1a and 3). The prograde equatorial and low-latitude jets represent the bulk of the surface gravity and generate positive gravity anomalies, deforming the planet in an oblate way, causing a non-negligible ΔJ_2. Moreover, the anomaly due to the GRS is well visible in the southern hemisphere in all three cases but its value saturates around 5 mGal even for very deep winds ($H_1, H_2 = 10^4$ km, see also Fig. 6). If the GRS penetrates deeper than the zonal winds (Fig. 7b, c, and f), the signature of the vortex emerges clearly in the map. If the jets are shallow (Fig. 7b and c), the background field disappears compared to the GRS anomaly.[3] On the contrary, when the jets are deeper than the vortices (Fig. 7d, g, and h) the gravity disturbance caused by the GRS disappears in the background field. In Section 6 we discuss the detectability of these various possibilities, with two different scale heights, given the measurement capabilities.

6. Detecting the GRS signature with the Juno gravity measurements

In this section we compare the intensity of the gravitational signature of the GRS, inferred by using our calculated gravity anomalies (Figs. 6 and 7), to the expected accuracies in the reconstruction of Jupiter's surface gravity by the *Juno* gravity experiment (Finocchiaro and Iess, 2010; Finocchiaro, 2013). This process involves the generation of synthetic radiometric data along a

---

[3] The latitudinal structures visible in the plots at the longitude of the GRS are due to the extension of the vortex high-velocity collar in the direction parallel to the spin axis, while spherical harmonics are referenced to the sphere.
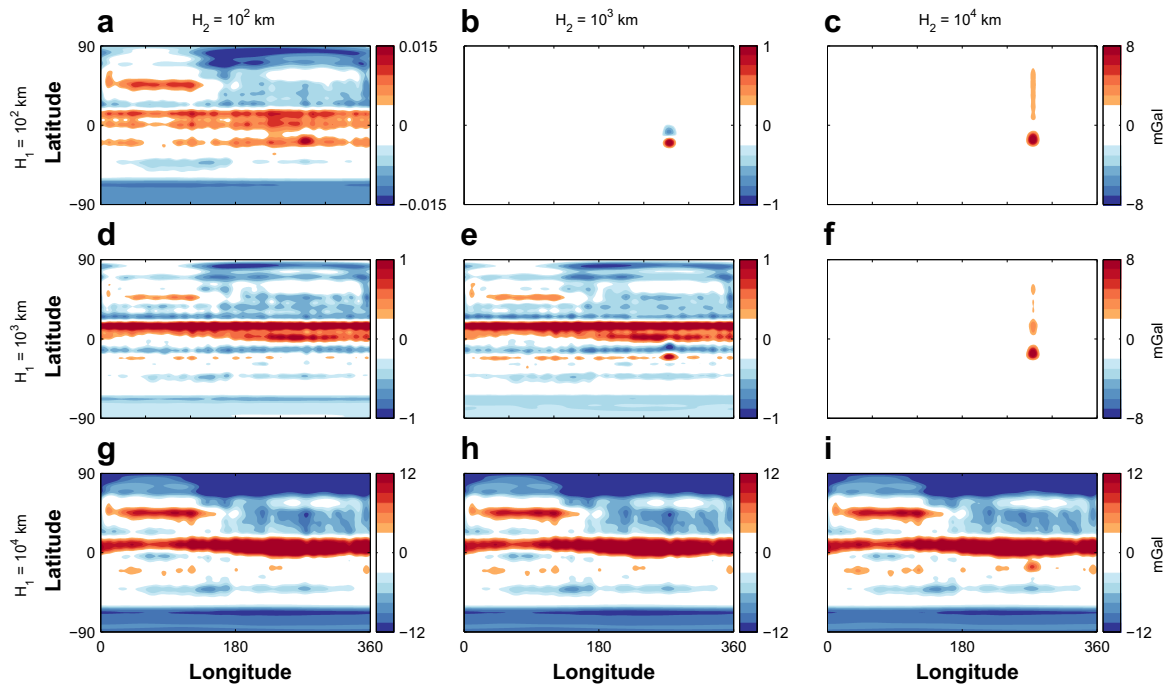
Fig. 7. Wind contributions to Jupiter' surface gravity, for different values of H_1 and H_2. The diagonal (panels a, e, and i) of the 3×3 matrix consists of the cases where $H_1 = H_2$ and gravity retraces the wind profiles. In the upper right (panels b, c, f) the GRS is deeper than the zonal winds and its gravitational signature is much stronger. Oppositely, in the lower left (panels d, g, and h) the jets are deeper and the axisymmetric signal obscures the GRS signature.

simulated trajectory, which is integrated including, in the dynamical model, the effect of the winds on Jupiter's gravity (Fig. 5). The synthetic data are processed into a least square multi-arc filter, which produces a formal covariance matrix for the estimation of physical parameters of interest, such as the spherical harmonic coefficients of Jupiter's gravitational potential expansion. The set of solve-for parameters is chosen to allow the fit of the Doppler residuals to the noise level. The number of estimated harmonics depends, in turn, on the strength of the winds (Finocchiaro, 2013), as discussed later on.

We first consider the case of uniform decay scale height for jets and vortices ($H_1 = H_2 = H$). The results of the comparison are showed in terms of: (i) the uncertainty $\sigma_{\Delta g}$ at the $1 - \sigma$ level (in mGal), in the retrieval of Jupiter's surface gravity with the *Juno* gravity experiment (Finocchiaro and Iess, 2010; Finocchiaro, 2013), in the proximity of the GRS and for different decay scale heights (Fig. 8a, c and e); and (ii) the non-dimensional ratio of the longitudinal variations of the surface gravity Δg, for the same decay scales, to the expected measurement accuracies $\sigma_{\Delta g}$ at close range to the GRS location (Fig. 8b, d and f). If the index, which we define as the signal to noise ratio (SNR), is smaller than unity, the signal of the gravity anomaly is weaker than the formal uncertainty, and therefore it will likely not be detectable.

For $H = 3 \times 10^2$ km, the GRS region, produce very shallow disturbances that perturb the underlying steady state only in the proximity of the planetary surface (Fig. 7a). The gravity field deviates mildly from that of a solid rotator and we expect very small tesseral harmonic coefficients due to the winds (Fig. 5a) when compared to the even-zonal contributions due to rotation (Hubbard, 2012). A 20×5 gravity field is sufficient to fit the simulated data (Finocchiaro, 2013), which yields an uncertainty map (Fig. 8a) that is nearly zonally symmetric everywhere and, in particular, with accuracies between 0.15 and 0.4 mGal in the proximity of the GRS. In this $30° \times 15°$ box, the gravity signal from the longitudinal variations of the winds is everywhere smaller than the measurement accuracy at the $1 - \sigma$ level (Fig. 8b), i.e., the SNR

is everywhere smaller than 1. In this case, the vortex is not deep enough to create mass anomalies detectable by the radio science instrument.

Winds characterized by a scale height of $H = 3 \times 10^3$ km represent the intermediate case where the penetration of the dynamics extends down to about 5% of Jupiter's mean radius. A much stronger atmospheric gravity signal is expected (Fig. 5b), involving also consistent longitudinal variations. Two concurring factors must be taken into account: on one hand, the gravity anomaly associated with the GRS is stronger because the winds are deeper and the gravity signal is a monotonic function of H (Fig. 6); on the other hand, the uncertainties also increase with H because of the higher-degree and order gravity field (20×15), and consequently the greater number of estimated parameters, necessary to fit the stronger simulated Doppler shift (Finocchiaro and Iess, 2010; Finocchiaro, 2013). The local uncertainties reach values of about 0.5 mGal (Fig. 8c), and show now longitudinal variations due, among other factors such as the degree and order of the expansion, to the expected ground tracks of the *Juno* spacecraft. At the same time, the GRS signal increases more steeply leading to a better SNR of about 4 within the high-velocity collar (Fig. 8d).

In the deep-wind case ($H = 10^4$ km), the winds affect consistently Jupiter's interior dynamics and penetrate deeply in the direction parallel to the spin axis. In the proximity of the GRS the uncertainty is growing again (Fig. 8e) due to the fact that a full 20×20 gravity field is needed to fit the simulated data. Nevertheless, the anomaly is still well above the 3-σ level around the GRS location, where the ratio reaches a peak of about 14 (Fig. 8f). The growth of the gravitational signature is still predominant when compared to the degradation in the estimation accuracies.

The three cases shown in Fig. 9 are examples of possible data analysis scenarios for the detection of the anomaly of the GRS, when varying the penetration depth of the winds. To further expand our analysis for uniform H, we carry out more simulations corresponding to scale heights ranging between $H = 10^2$ km and
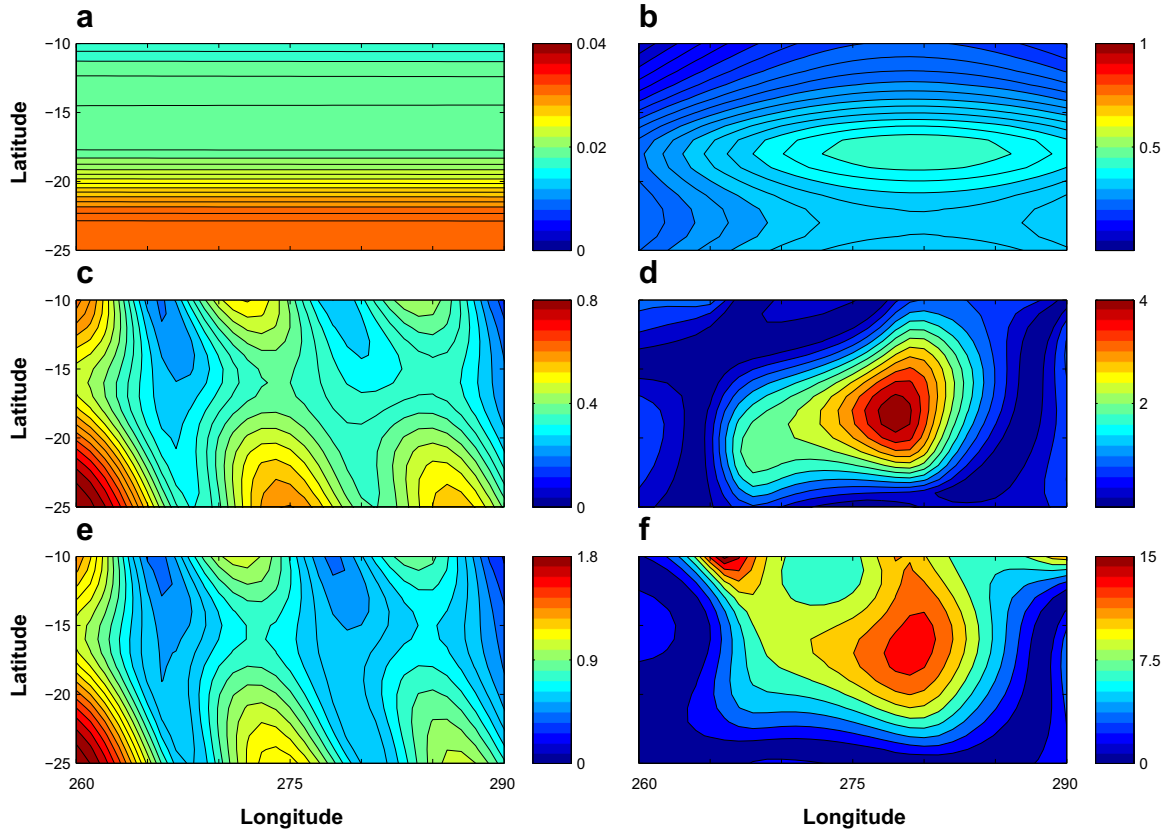
Fig. 8. Maps of the measurement uncertainties for the surface gravity of Jupiter in the neighborhood of the GRS (panels a, c and e), in mGal. Ratio of the GRS gravity anomaly to the local formal uncertainty at the 1-σ level (panels b, d and f), adimensional. The plots are also divided by different scale height: $H = 3 \times 10^2$ km (a and b), the magnitude of the gravity signal is everywhere below 3-σ in the proximity of the vortex; $H = 3 \times 10^3$ km (c and d), the GRS anomaly is well visible in the southern hemisphere, with a maximum signal to noise ratio of 3.7; $H = 10^4$ km (e and f), the gravity signal from the GRS is about 14 times larger than the expected formal uncertainty.

10^4 km. For each value of H the number of solve-for parameters is optimized according to Finocchiaro (2013). Fig. 9 shows the ratio of the surface gravity at the GRS coordinates (22°S and 274°) to the correspondent uncertainty as a function of the scale height, on a logarithmic scale. The gravitational signature of the vortex is at least 3 times stronger than the localized measurement accuracy for values of H larger than about 2×10^3 km. The SNR increases then monotonically for 2×10^3 km $< H < 10^4$ km.

In order to cover a broader range of possibilities, we repeat the same analysis for $H_1 \neq H_2$. In this case it is necessary to consider all different combinations of the jet scale height and the vortex scale height. As before, for each choice of H_1 and H_2, the best (smallest) set of estimated spherical harmonics is chosen, capable of fitting the simulated Doppler residuals (Finocchiaro and Iess, 2010; Finocchiaro, 2013). The result is a matrix of the GRS detectability (Fig. 10), whose main diagonal represents the cases already studied
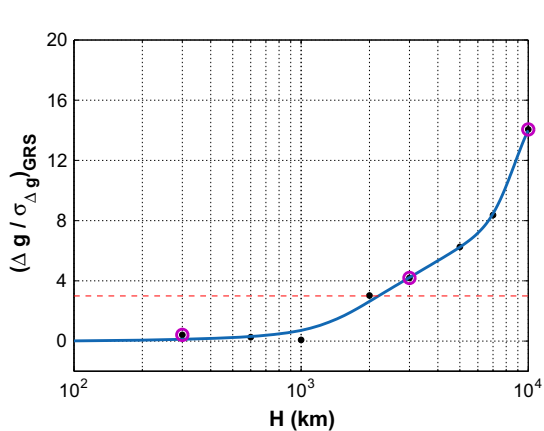
Fig. 9. The ratio of the surface acceleration at the GRS location to the formal measurement uncertainty, as a function of the scale height H. The plot is semi-logarithmic on the x-axis. The ratio is above the value of 3 for decay scale heights larger than 2,000 km. The purple circles represent the three cases shown in Fig. 8b, d and f.
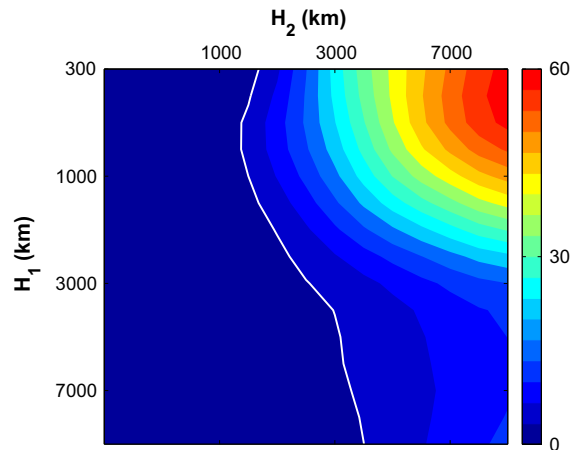
Fig. 10. Matrix of the detectability of the GRS as a function of the jet scale height H_1 and the vortex scale height H_2. Values larger than 3 (right of the white contour) identify the domain in which the gravity anomaly is at least 3 times larger than the expected measurement accuracy.

of $H_1 = H_2$ (Fig. 9). The ratio of the predicted gravity anomaly of the GRS to the expected accuracy in the determination of the local surface gravity is still the chosen quantity to identify the combinations of (H_1, H_2) for which it is theoretically possible to detect the gravitational signature of the vortex (Fig. 10). We notice that, when the vortex scale height is larger than the jet scale height ($H_1 < H_2$, in Fig. 10, right of the main diagonal), the signal to noise ratio at the GRS location can become very large (values up to 75), especially if the scale height characterizing the jets is very small, because fewer parameters are necessary to fit the simulated Doppler residuals (Finocchiaro and Iess, 2010; Finocchiaro, 2013) and the vortex is very deep. On the contrary, left of the main diagonal the jets are much deeper than the vortices causing the gravity anomaly of the GRS to blend into the background surface gravity, making the detection of its signature highly improbable.

7. Conclusion

The resemblance of the GRS to coherent atmospheric features we observe on Earth leads to thinking that it is a shallow atmospheric structure resulting from 2D turbulence as we observe cyclones and anticyclones on Earth. On the other hand, the fact that it exists for over 300 years hints that enough mass is involved so it will not be sheared apart by the surrounding turbulent jets, and therefore leads to the thinking that it is a deeply rooted feature. Understanding this puzzle has implications, not only for the vertical structure and energetics of the GRS itself, but for a better understanding of the planet's interior structure, dynamics and evolution which are all tied due to the constraints provided by the gravity harmonics. In this work, we study the possibility of detecting the GRS gravitational signature and, consequently, infer its depth, using simulated gravity measurements of the upcoming *Juno* mission.

The method entails solving a set of partial differential equations relating the velocity field of Jupiter to the distribution of the density anomalies caused by the wind motion. We assume that Jupiter's large-scale atmospheric dynamics are, to leading order, in thermal wind balance and produce three-dimensional maps of the density fluctuations, depending on the e-folding depth scale of the winds. We find that longitudinal and latitudinal small-scale features, such as the GRS, emerge in the gravity field, if the differential equations are integrated over a two-dimensional grid, considering both zonal and meridional components of the wind velocity. We find that as the mass involved in atmospheric flows increases, the gravity signal coming from the winds becomes stronger and the tesseral perturbations are larger. We explore the resulting gravity field also for cases in which the depth of the GRS is different from the depth of the large scale flow. We found that its signal in the gravity field is more evident in cases where the depth of the GRS is larger than the depth of the mean flow.

Once the contributions of the winds to Jupiter's gravity are predicted by means of theoretical models, it is possible to compare the results to the expected accuracies in the reconstruction of the planetary surface gravity (Finocchiaro and Iess, 2010; Finocchiaro, 2013). If the jets and the vortices are characterized by the same scale height, we conclude that there is a quite well-defined value of H (2,000 km) beyond which the signal to noise ratio is large enough (>3) to be detected by the *Juno* radio science instrumentation. The results are interpreted in view of two counteracting effects: the growth of the GRS signal due to the increase in the mass involved in the wind motions, and the degradation of the measurement accuracies due to different analysis setups (Finocchiaro and Iess, 2010; Finocchiaro, 2013).

However, the zonal jets and the tesseral perturbations might not extend to the same pressure level. Depending on the combination of the two e-folding scales, the gravitational signature of the GRS can either stand out or dissolve in the background almost-zonal gravity field. Our simulations show that, if the GRS atmospheric dynamics are characterized by a scale height much larger than the zonal jets, then the chances of detecting its gravitational signature increase significantly (Fig. 10). On the other hand, if the jets are very deep, the detection is much less likely for two main reasons: the gravity signal of the jets becomes comparable to that of the GRS and the number of parameters necessary to fit the Doppler residuals is larger.

The *Juno* sensitivity results presented in this paper are dependent on the model adopted in the spacecraft orbit determination process. In our simulations, some small non-gravitational forces (e.g., Jupiter infrared emission and its the latitudinal variation) have not been accounted for, because their effect has been assessed as negligible in previous work (Finocchiaro and Iess, 2010). However, we point out that acoustic global modes of Jupiter, as detected by Gaulme et al. (2011) using SYMPA data, can interfere with the correct retrieval of the planet's spherical harmonic coefficients and are therefore of particular concern. If these oscillations are indeed present at the amplitude suggested by the SYMPA observations, we may expect variations in the shape of Jupiter of about 50–80 m at frequencies between 800 and 2100 Hz and between 2400 and 3400 Hz (Gaulme et al., 2011). These oscillations in the shape of the planet will generate a dynamical component of Jupiter's gravity field, that may interfere with the retrieval of the static and tidal components of the gravitational potential, as well, of course, with the determination of the gravity perturbation from the GRS. When dealing with the reconstruction of the surface gravity one has to keep in mind the correlation and overlapping of the different components of the gravity field.

Nonetheless, despite the uncertainty in the measurement capabilities prior to the arrival of *Juno* at Jupiter, this study provides the first estimates of what might be the tesseral field of Jupiter resulting from dynamics. Beyond detection of the GRS signature itself, this tesseral field is important for the reconstruction of the Juno data (Finocchiaro, 2013), and here we provide order-of-magnitude estimates for this field (Fig. 5). Moreover, the estimate of the tesseral harmonic coefficients provided by the study shows that the low tesseral field (e.g., C_{22}) will be competing with the signal induced by tides, mainly by Io. Thus, depending on the depth of the flows and the longitudinal fluctuation of the wind field, the wind-induced tesseral gravity field might obscure the detection of tide-induced tesserals, and therefore it is very important to constrain this field and provide an estimate from theoretical models. As the data arrives, future studies will be able to further interpret the tesseral field, with the challenge of inverting it into meaningful physical quantities. In summary, the tesseral gravity field, which this study is the first to address, may hold important information regrading the dynamics and interior structure of the planet, and the interpretation of this signal will be a grand challenge in the upcoming years.

Appendix A. Integration of thermal wind equations

Starting from system (3), we wish to derive the second-order cross-derivative from each equation:

$$\begin{cases} \frac{\partial}{\partial\phi}\left(\frac{\partial\rho'}{\partial\theta}\right) = \frac{\partial}{\partial\phi}\left(\frac{2\Omega}{g_0}r\frac{\partial\tilde{\rho}u}{\partial z}\right), \\ \frac{\partial}{\partial\theta}\left(\frac{\partial\rho'}{\partial\phi}\right) = \frac{\partial}{\partial\theta}\left(-\frac{2\Omega}{g_0}r\sin\theta\frac{\partial\tilde{\rho}v}{\partial z}\right), \end{cases} \tag{A.1}$$

where for convenience, despite working in spherical coordinates, we use $\partial/\partial z$ where z is the direction parallel to the axis of rotation. This partial derivative can be opened in spherical coordinates to be:

$$\frac{\partial}{\partial z} = \cos\theta\frac{\partial}{\partial r} - \sin\theta\frac{\partial}{\partial\theta}. \tag{A.2}$$

All other symbols have been defined in Section 2. If the density anomaly is a C^2 function (second derivatives existing and continuous), the cross derivatives are equivalent and the two equations can be summed up:

$$2\frac{\partial^2\rho'}{\partial\phi\partial\theta} = \frac{\partial}{\partial\phi}\left(\frac{2\Omega}{g_0}r\frac{\partial\tilde{\rho}u}{\partial z}\right) - \frac{\partial}{\partial\theta}\left(\frac{2\Omega}{g_0}r\sin\theta\frac{\partial\tilde{\rho}v}{\partial z}\right). \tag{A.3}$$

Eq. (A.3) can be integrated a first time with respect to θ:

$$\frac{\partial\rho'}{\partial\phi} = \frac{1}{2}\int\frac{\partial}{\partial\phi}\left(\frac{2\Omega}{g_0}r\frac{\partial\tilde{\rho}u}{\partial z}\right)d\theta - \frac{1}{2}\left(\frac{2\Omega}{g_0}r\sin\theta\frac{\partial\tilde{\rho}v}{\partial z}\right) + f_0'(r,\phi), \tag{A.4}$$

and a second time with respect to ϕ:

$$\rho' = \frac{1}{2}\int\left(\frac{2\Omega}{g_0}r\frac{\partial\tilde{\rho}u}{\partial z}\right)d\theta - \frac{1}{2}\int\left(\frac{2\Omega}{g_0}r\sin\theta\frac{\partial\tilde{\rho}v}{\partial z}\right)d\phi + \int f_0'(r,\phi)d\phi + \rho_1'(r,\theta), \tag{A.5}$$

where $\int f_0'(r,\phi)d\phi$ is still a function of r and ϕ, hence:

$$\rho'(r,\theta,\phi) = \frac{1}{2}\int\left(\frac{2\Omega}{g_0}r\frac{\partial\tilde{\rho}u}{\partial z}\right)d\theta - \frac{1}{2}\int\left(\frac{2\Omega}{g_0}r\sin\theta\frac{\partial\tilde{\rho}v}{\partial z}\right)d\phi + \rho_2'(r,\phi) + \rho_1'(r,\theta). \tag{A.6}$$

In order to calculate the two constants of integration, we must impose two boundary conditions. The first one is that, for $v \to 0$, the expression for the density perturbation must converge to its expression for the purely zonal case (Kaspi et al., 2010). Suppose that the u component of the velocity can be expressed as the sum of two different contributions: one that depends only on depth and colatitude: $\bar{u}(r,\theta)$; and one that depends only on longitude: $u'(\phi)$. Then:

$$\lim_{v\to 0}\rho'(r,\theta,\phi) = \int\left(\frac{2\Omega}{g_0}r\frac{\partial\tilde{\rho}\bar{u}(r,\theta)}{\partial z}\right)d\theta + \rho_3'(r). \tag{A.7}$$

When $v \to 0$, u tends to $\bar{u}$, because u cannot be a function of the longitude for Eq. (3):

$$\lim_{v\to 0}u(r,\theta,\phi) = \bar{u}(r,\theta). \tag{A.8}$$

Also, the following expressions:

$$\begin{aligned} u(r,\theta,\phi) &\to \bar{u}(r,\theta), \\ v &\to 0, \\ u'(\phi) &\to 0, \end{aligned} \tag{A.9}$$

are equivalent. Using the general expression for the density perturbation (A.6), the limit in (A.7) becomes:

$$\lim_{v\to 0}\frac{1}{2}\int\left(\frac{2\Omega}{g_0}r\frac{\partial\tilde{\rho}u}{\partial z}\right)d\theta - \lim_{v\to 0}\frac{1}{2}\int\left(\frac{2\Omega}{g_0}r\sin\theta\frac{\partial\tilde{\rho}v}{\partial z}\right)d\phi + \lim_{v\to 0}\left[\rho_2'(r,\phi) + \rho_1'(r,\theta)\right] = \int\left(\frac{2\Omega}{g_0}r\frac{\partial\tilde{\rho}\bar{u}(r,\theta)}{\partial z}\right)d\theta + \rho_3'(r), \tag{A.10}$$

whence:

$$\frac{1}{2}\int\left(\frac{2\Omega}{g_0}r\frac{\partial\tilde{\rho}\bar{u}}{\partial z}\right)d\theta + \lim_{v\to 0}\left(\rho_2'(r,\phi) + \rho_1'(r,\theta)\right) = \int\left(\frac{2\Omega}{g_0}r\frac{\partial\tilde{\rho}\bar{u}}{\partial z}\right)d\theta + \rho_3'(r), \tag{A.11}$$

and consequently:

$$\lim_{v\to 0}\left[\rho_2'(r,\phi) + \rho_1'(r,\theta)\right] = \frac{1}{2}\int\left(\frac{2\Omega}{g_0}r\frac{\partial\tilde{\rho}\bar{u}}{\partial z}\right)d\theta + \rho_3'(r), \tag{A.12}$$

At this point a few considerations are in order. Since ρ_1' is only a function of r and θ, this constant of integration can only depend on the components of u and v that don't depend on the longitude, $\bar{u}$ and $\bar{v}$. However $\bar{v} = 0$, because the v component of the velocity must be zero-average over longitude, otherwise there would be a net flux in the latitudinal direction. Hence $\rho_1' = \rho_1'(r,\theta,\bar{u})$, and it cannot be affected by v disappearing. As a consequence, from (A.12) an expression for ρ_1' is now available:

$$\rho_1'(r,\theta) = \frac{1}{2}\int\left(\frac{2\Omega}{g_0}r\frac{\partial\tilde{\rho}\bar{u}(r,\theta)}{\partial z}\right)d\theta + \rho_3'(r) - \lim_{v\to 0}\rho_2'(r,\phi). \tag{A.13}$$

Furthermore, for the second equation of system (3), when $v \to 0$, the density perturbation can only be a function of θ, thus:

$$\lim_{v\to 0}\rho_2'(r,\phi) = \rho_4'(r). \tag{A.14}$$

Applying the first boundary condition, one of the constants has been determined and put into the general expression for ρ':

$$\rho'(r,\theta,\phi) = \frac{1}{2}\int\left(\frac{2\Omega}{g_0}r\frac{\partial\tilde{\rho}u(r,\theta,\phi)}{\partial z}\right)d\theta - \frac{1}{2}\int\left(\frac{2\Omega}{g_0}r\sin\theta\frac{\partial\tilde{\rho}v(r,\theta,\phi)}{\partial z}\right)d\phi + \frac{1}{2}\int\left(\frac{2\Omega}{g_0}r\frac{\partial\tilde{\rho}\bar{u}(r,\theta)}{\partial z}\right)d\theta + \rho_2'(r,\phi), \tag{A.15}$$

where $\rho_3'(r)$ and $\rho_4'(r)$ have been incorporated into $\rho_2'(r,\phi)$. Eq. (A.15) appears therefore in Section 2 as Eq. (9).

References

Asay-Davis, X.S. et al., 2009. Jupiter's shrinking Great Red Spot and steady Oval BA: Velocity measurements with the 'Advection Corrected Correlation Image Velocimetry' automated cloud-tracking method. Icarus 203, 164–188.

Busse, F.H., 1976. A simple model of convection in the Jovian atmosphere. Icarus 29, 255–260.

Choi, D.S., Showman, A.P., 2011. Power spectral analysis of Jupiter's clouds and kinetic energy from Cassini. Icarus 216, 597–609.

Choi, D.S. et al., 2007. Velocity and Vorticity Measurements of Jupiter's Great Red Spot Using Automated Cloud Feature Tracking. Icarus 188, 35–46.

Dowling, T.E., Ingersoll, A.P., 1988. Potential Vorticity and Layer Thickness Variations in the Flow around Jupiter's Great Red Spot and White Oval BC. J. Atmos. Sci. 45 (8), 1380–1396.

Dowling, T.E., Ingersoll, A.P., 1989. Jupiter's Great Red Spot as a Shallow Water System. J. Atmos. Sci. 46 (21), 3256–3278.

Finocchiaro, S., 2013. Numerical Simulations of the Juno Gravity Experiment. Ph.D. Thesis. Pubblicazioni Aperte Digitali della Sapienza. Code 1889.

Finocchiaro, S., Iess, L., 2010. Numerical simulations of the gravity science experiment of the Juno mission to Jupiter. Space Flight Mechanics 2010, vol. 136. American Astronomical Society, pp. 1417–1426.

Galanti, E., Kaspi, Y., 2015. Deciphering Jupiter's complex flow dynamics using the upcoming Juno gravity measurements and an adjoint based dynamical model. 47th Meeting of the Division for Planetary Science, 403.08.

Gaulme, P. et al., 2011. Detection of jovian seismic waves: A new probe of its interior structure. Astron. Astrophys. 531, A104.

Guillot, T., Morel, P., 1995. CEPAM: A code for modeling the interiors of giant planets. Astron. Astrophys., Suppl. Ser. 109, 109–123.

Hubbard, W.B., 1999. Gravitational Signature of Jupiter's Deep Zonal Flows. Icarus 137, 357–359.

Hubbard, W.B., 2012. High-precision Maclaurin-based models of rotating liquid planets. Astrophys. J. 756, L15.

Hubbard, W.B., 2013. Concentric Maclaurin spheroid models of rotating liquid planets. Astrophys. J. 768 (1), 43–50.

Ingersoll, A.P., Pollard, D., 1982. Motion in the interiors and atmospheres of Jupiter and Saturn: scale analysis, anelastic equations, barotropic stability criterion. Icarus 52, 62–80.

Kaspi, Y., 2008. Turbulent Convection in Rotating Anelastic Spheres: A Model for the Circulation on the Giant Planets. Ph.D. Thesis. Massachusetts Institute of Technology.

Kaspi, Y., 2013. Inferring the depth of the zonal jets on Jupiter and Saturn from odd gravity harmonics. Geophys. Res. Lett. 40, 676–680.

Kaspi, Y., Flierl, G.R., Showman, A.P., 2009. The deep wind structure of the giant planets: Results from an anelastic general circulation model. Icarus 202, 525–542.

Kaspi, Y. et al., 2010. Gravitational signature of Jupiter's internal dynamics. Geophys. Res. Lett. 37, L01204.

Kaspi, Y. et al., 2013. Atmospheric confinement of jet streams on Uranus and Neptune. Nature 497, 344–347.

Kong, D. et al., 2013. Gravitational signature of rotationally distorted Jupiter caused by deep zonal winds. Icarus 226, 1425–1430.

Lian, Y., Showman, A.P., 2008. Deep jets on gas-giant planets. Icarus 194, 597–615.

Liu, J., Schneider, T., 2010. Mechanisms of Jet Formation on the Giant Planets. J. Atmos. Sci. 67, 3652–3672.

Liu, J., Schneider, T., Kaspi, Y., 2013. Predictions of thermal and gravitational signals of Jupiter's deep zonal winds. Icarus 224, 114–125.

Morales-Juberias, R., Dowling, T.E., 2013. Jupiter's Great Red Spot: Fine-scale matches of model vorticity patterns to prevailing cloud patterns. Icarus 225, 216–227.

Pedlosky, J., 1987. Geophysical Fluid Dynamics. Springer.

Rhines, P.B., 1979. Geostrophic turbulence. Annu. Rev. Fluid Mech. 11, 401–441.

Schneider, T., Liu, J., 2009. Formation of Jets and Equatorial Superrotation on Jupiter. J. Atmos. Sci. 66, 579–601.

Showman, A.P., Gierasch, P.J., Lian, Y., 2006. Deep zonal winds can result from shallow driving in a giant-planet atmosphere. Icarus 182, 513–526.

Simon, A.A. et al., 2014. Dramatic change in Jupiter's Great Red spot from spacecraft observations. Astrophys. J. 797, L31.

Vasavada, A.R., Showman, A.P., 2005. Jovian atmospheric dynamics: an update after Galileo and Cassini. Rep. Prog. Phys. 68, 1935–1996.

West, R.A., Tomasko, M.G., 1980. Spatially resolved methane band photometry of Jupiter: III. Cloud vertical structures for several axisymmetric bands and the Great Red Spot. Icarus 41, 278–292.

Yano, J., Flierl, G.R., 1994. Jupiter's Great Red Spot: compactness condition and stability. Ann. Geophys. 12, 1–18.

Young, R.E., 1998. The Galileo probe mission to Jupiter: Science overview. J. Geophys. Res. 103 (E10), 775–790.

Zhang, K., Kong, D., Schubert, G., 2015. Thermal-gravitational wind equation for the wind-induced gravitational signature of giant gaseous planets: Mathematical derivation, numerical method and illustrative solutions. Astrophys. J. 806, 270–279.